PHYSICAL REVIEW FLUIDS **5**, 124001 (2020)

Rivulet cascade from falling liquid films with side contact lines

G. Lavalle,[*] J. Sebilleau, and D. Legendre
Institut de Mécanique des Fluides de Toulouse (IMFT) - Université de Toulouse, CNRS-INPT-UPS, 31400 Toulouse, France

(Received 18 January 2020; accepted 4 November 2020; published 2 December 2020)

We investigate the dynamics of films of partially wetting liquids falling down a vertical plane in the presence of air. We focus on the little-studied case where the film is not in contact with lateral walls and thus has two side contact lines. By way of 3D direct numerical simulations, we study the fingering instability and the distribution of rivulets. Our results show that the instability develops as a cascade: two twin rivulets first develop at the free sides, followed by a series of twin rivulets growing closer to the center. This self-sustained fall is caused by the formation of stagnation zones at the front contact line as the liquid behind the ridge escapes toward a newly created rivulet. We also show that the established rivulet distance follows the prediction of linear instability, despite the cascade. The dynamics of the cascade is modified by inertial and film thickness effects, as well as by initial shape perturbations of the contact line. On the contrary, varying the contact angle does not affect the development of the cascade, apart from the average wavelength.

DOI: 10.1103/PhysRevFluids.5.124001

I. INTRODUCTION

Liquid rivulets are streamlets bounded by two contact lines. These elongated fluid structures are commonly observed in our daily life, e.g., on shower glass or house or car windows. In addition, they have a strong impact on multiple technological applications. For instance, rivulet flows might degrade the aerodynamic efficiency of wings in rain (Thompson and Jang [1]) or the wall coating.

When a thin liquid film falls down an inclined or vertical dry plate, a capillary ridge develops behind the advancing contact line. A front instability occurs when the ridge is sufficiently pronounced, and finger-like liquid structures develop as thicker regions progress faster than thinner regions (Spaid and Homsy [2], Bonn *et al.* [3]). This was clearly observed experimentally (Huppert [4], Silvi and Dussan [5], Jerrett and de Bruyn [6], de Bruyn [7], Johnson *et al.* [8]). Subject to different flow and substrate conditions, the fingering instability might evolve into more elaborated liquid structures governed by nonlinear interactions, which we refer to as rivulets.

We now discuss those works related to the numerical analysis of gravity-driven films of fully/partially wetting fluids.

By employing a lubrication model with precursor film, Kondic and Diez [9] analyzed the effect of initial sinusoidal perturbations of the contact line on the fingering instability. When the domain width is comparable to the most unstable wavelength obtained via linear instability, they concluded that perturbations outside the band of unstable wavelengths decay, whereas those within the unstable band are characterized by several different growth rates. Subsequently, Ledesma-Aguilar *et al.* [10] used the lattice-Boltzmann method to study the effect of sinusoidal, parabolic, and finger-like initial

[*]Present address: Mines Saint-Etienne, Université de Lyon, CNRS, UMR 5307 LGF, Centre SPIN, Department PEG, F-42023 Saint-Etienne, France; gianluca.lavalle@imft.fr

conditions and of system width on the finger pattern. They found that the solution is not sensitive to the employed initial condition, and that the width of the system mainly affects the rivulet distance.

In another study, by employing a lubrication model with precursor film, Diez and Kondic [11] argued that complete coating of the surface is to be expected for fully wetting fluids and that only partially wetting fluids might lead to incomplete coverage. This issue was addressed also by Moyle *et al.* [12], who performed time-dependent simulations of partially wetting fluids showing that troughs are stationary when the contact slope $C = (3\mathrm{Ca})^{-1/3}\tan\theta > 1$, where Ca is the capillary number and θ the contact angle.

Other features of fully nonlinear simulations of the fingering instability have also received a lot of attention, such as the rivulet breakup (Eres *et al.* [13], Ledesma-Aguilar *et al.* [14]), the effect of the inclination angle (Kondic and Diez [9]) and of the contact angle (Sebastia-Saez *et al.* [15]) on the nonlinear dynamics, as well as the influence of surface heterogeneities (Kondic and Diez [16], Marshall and Wang [17], Slade *et al.* [18]).

All the above-mentioned works focus on films in contact with sidewalls and are characterized by a front contact line. The effect of lateral contact lines was first investigated by Lan *et al.* [19], both numerically (by means of the volume of fluid method) and experimentally. In this configuration, surface tension effects lead to the contraction of the film in the spanwise direction. The authors discussed the decrease in film width by varying several parameters, such as Reynolds number and contact angle. Their scenario is such that a single central flow takes place without rivulet occurrence. This has prompted us in studying how the finger instability develops in the presence of restriction of the film width and how the general flow pattern changes under the effect of initial conditions and contact-line perturbations. Thus, the problem studied in this paper is similar to the work of Lan *et al.* [19], except that the flow conditions considered here lead to a significantly different flow pattern, with formation of rivulets.

Subsequently, Thoraval *et al.* [20] studied experimentally a vertical falling film of partially wetting fluid and reported the formation of two lateral rivulets during the transient states. This was also confirmed by Lallement [21] by employing a long-wave shallow water model with precursor film.

Our current work investigates the dynamics and distribution of rivulets originating from liquid films driven by gravity on vertical planes. Based on direct numerical simulations (DNSs), we aim at studying the scenario where the liquid film is not in contact with sidewalls and thus has two lateral contact lines, as sketched in Fig. 1. We are particularly interested in the wavelength selection and in the influence of contact-line shape perturbations, inertia, film thickness, and contact angle.

The article is structured as follows. In Sec. II we write the governing equations and describe the numerical approach (some specific validations for the simulation of falling liquid films are reported in the Appendix). In Sec. III we present the rivulet cascade and describe the mechanism responsible for the cascade-like instability of the contact line. Section IV is devoted to the discussion of the wavelength selection with respect to the prediction of linear instability. Concluding remarks are presented in Sec. V.

II. GOVERNING EQUATIONS AND EMPLOYED NUMERICAL METHOD

A. Governing equations

We consider a three-dimensional liquid film of partially wetting fluids falling down an inclined or vertical wall in interaction with an upper gaseous phase (Fig. 1). Under the assumption of Newtonian incompressible and isothermal fluids, and neglecting the phase change, the full dynamics of the considered two-phase flow is subject to the three-dimensional Navier-Stokes equations:

$$\nabla\cdot\mathbf{u}_l = 0, \qquad \nabla\cdot\mathbf{u}_g = 0, \tag{1a}$$

$$\rho_l(\partial_t\mathbf{u}_l + \mathbf{u}_l\cdot\nabla\mathbf{u}_l) = -\nabla p_l + \rho_l\mathbf{g} + \mu_l\Delta\mathbf{u}_l\,, \tag{1b}$$

$$\rho_g(\partial_t\mathbf{u}_g + \mathbf{u}_g\cdot\nabla\mathbf{u}_g) = -\nabla p_g + \rho_g\mathbf{g} + \mu_g\Delta\mathbf{u}_g\,, \tag{1c}$$

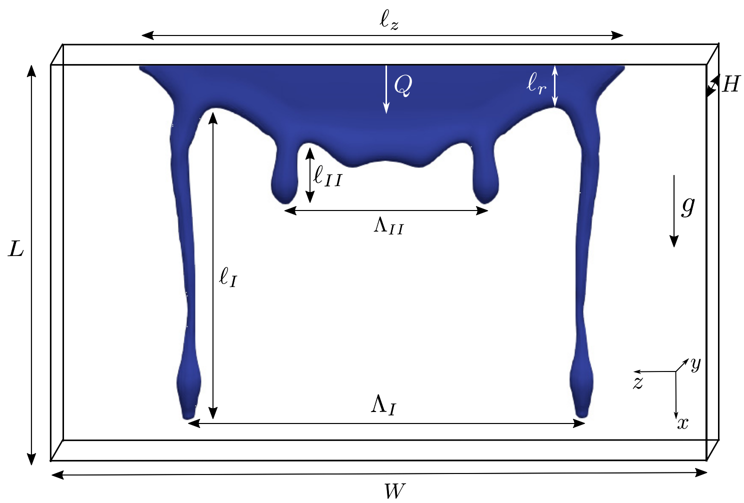

FIG. 1. Sketch of the considered problem and used notations: a film of partially wetting fluid with side contact lines down a vertical plane in contact with air.

where l, g are phase indicators, ∇ the nabla operator, and Δ the Laplace operator. Also, $\mathbf{u} = (u, v, w)$ represents the velocity along the streamwise, cross-stream, and spanwise directions (x, y, z), p the pressure, $\mathbf{g} = (g \sin\beta, -g\cos\beta, 0)$ the gravity with the inclination angle β, and ρ, μ density and viscosity.

Equations (1) are completed with boundary conditions at the interface:

$$\mathbf{n} \cdot [\Sigma] \cdot \mathbf{n} = \gamma \nabla \cdot \mathbf{n}\,, \tag{2a}$$

$$\mathbf{n} \cdot [\Sigma] \cdot \mathbf{t} = 0, \tag{2b}$$

where $\mathbf{n}, \mathbf{t}$ are the tangent and normal unit vectors to the interface, Σ the stress tensor, and γ the surface tension. The symbol $[\cdot]$ identifies the jump at the interface.

At the moving contact line, where the three phases interact, the no-slip condition leads to a diverging energy dissipation (Huh and Scriven [22], Bonn *et al.* [3]). Several models have been developed to mitigate the stress singularity paradox, as the precursor film and the Navier slip models. In this work, the Cox-Voinov hydrodynamical model is employed (Voinov [23], Cox [24]), and its incorporation within the numerical procedure will be detailed in the next section.

B. Numerical method

Our direct numerical simulations were performed with the flow solver JADIM (Magnaudet *et al.* [25]), which was been successfully employed for disperse two-phase flows, bubble dynamics, and sliding drop (Legendre and Magnaudet [26], Bonometti and Magnaudet [27], Dupont and Legendre [28]). This is a finite volume solver based on the volume of fluid (VOF) (Hirt and Nichols [29]) and continuum surface force (CSF) (Brackbill *et al.* [30]) methods. The liquid-gas interface is computed with the flux-corrected transport (FCT) method (Zalesak [31]) by means of an accurate transport algorithm. This algorithm allows us to preserve the stiffness of the fronts while keeping the numerical thickness of the interface within three grid cells (Bonometti and Magnaudet [27]).

The VOF method consists of solving the Navier-Stokes equations (1) for a single fluid on a fixed grid:

$$\partial_t \varphi + \mathbf{u} \cdot \nabla \varphi = 0, \tag{3a}$$

$$\nabla \cdot \mathbf{u} = 0, \tag{3b}$$

$$\rho(\partial_t \mathbf{u} + \mathbf{u} \cdot \nabla \mathbf{u}) = -\nabla p + \rho \mathbf{g} + \nabla \cdot \mathbf{T} + F_s, \tag{3c}$$

where φ is the volume fraction ($\varphi = 1$ in cells with liquid only and $\varphi = 0$ in cells with gas only), $\mathbf{T}$ the viscous stress tensor, and F_s the capillary contribution to the normal coupling condition. The single-fluid properties are obtained through a linear interpolation based on φ:

$$\rho = \varphi \rho_l + (1 - \varphi)\rho_g, \qquad \mu = \varphi \mu_l + (1 - \varphi)\mu_g, \tag{4}$$

$$\mathbf{u} = \varphi \mathbf{u}_l + (1 - \varphi)\mathbf{u}_g, \qquad p = \varphi p_l + (1 - \varphi)p_g. \tag{5}$$

With the CSF formulation, the capillary contribution in (3) takes the form

$$F_s = -\gamma \, \nabla \cdot \left(\frac{\nabla \varphi}{|\nabla \varphi|} \right) \nabla \varphi. \tag{6}$$

Since our approach does not rely on the interface reconstruction, computing (6) requires to know $\nabla \varphi$. At the wall, $\nabla \varphi$ and the contact angle θ are related through

$$\mathbf{n} = \frac{\nabla \varphi}{|\nabla \varphi|} = \sin \theta \, \mathbf{n}_{wt} + \cos \theta \, \mathbf{n}_{wn}, \tag{7}$$

where $\mathbf{n}_{wt}$ and $\mathbf{n}_{wn}$ are the tangent and normal unit vectors to the wall (Dupont and Legendre [28], Mohand *et al.* [32]).

The value of the contact angle is determined through the Cox-Voinov hydrodynamic model, which relates the static contact angle θ_s controlled by intermolecular forces in the microscopic region to the *dynamic* contact angle θ, which has a logarithmic evolution with the distance to the contact line. The distance of observation for a computational fluid dynamics (CFD) simulation is imposed by the grid size. Indeed, the physics smaller than the grid size cannot be solved and need to be modeled. In the model originally proposed by Dupont and Legendre [28], the imposed dynamic contact angle θ makes use of the Cox-Voinov relation with the grid size Δ representing the distance to the contact line:

$$g(\theta) = g(\theta_s) + \mathrm{Ca}_{cl} \ln \left(\frac{\Delta/2}{l} \right), \tag{8}$$

in which $l \simeq 1$ nm represents the microscopic length scale where the intermolecular forces dominate, and $\mathrm{Ca}_{cl} = \mu_l U_{cl} \gamma^{-1}$ the contact-line capillary number based on the contact-line velocity U_{cl}. The value of U_{cl} is obtained from the interpolation of the interface velocity at $\varphi = 0.5$ at the distance $\Delta/2$ from the wall (Dupont and Legendre [28], Legendre and Maglio [33]). For gas-liquid flows, the function $g(\theta)$ can be simplified to

$$g(\theta) = \int_0^\theta \frac{\vartheta - \sin \vartheta \cos \vartheta}{2 \sin \vartheta} \, d\vartheta. \tag{9}$$

When $\theta < 3/4\pi$, the Cox-Voinov dynamic model (8) and (9) can be approximated as $\theta^3 = \theta_s^3 + 9\,\mathrm{Ca}_{cl} \ln(\Delta/2\,l)$. At this point, the angle is used for the calculation of the capillary contribution (7) in the momentum balance (3) (Dupont and Legendre [28]).

The discretization of Eqs. (3) is performed on a staggered mesh with second-order accuracy in space. Time discretization is performed through a third-order Runge-Kutta method for the viscous terms. Incompressibility is satisfied at the end of each time step by solving the pseudo-Poisson equation.

TABLE I. Physical properties of the working liquids considered in the numerical study.

Fluid	Type	ρ_l (kg m^{-3})	ν_l (m^2 s^{-1})	ρ_g (kg m^{-3})	ν_g (m^2 s^{-1})	γ (mN m^{-1})
A	water/glycerin (80%), air	1190	2.44×10^{-5}	1.25	1.5×10^{-5}	64
B	water/glycerin (50%), air	1130	5.02×10^{-6}	1.25	1.5×10^{-5}	69

C. Numerical setup

The numerical results presented in the paper are all obtained with two working liquids: (A) a mixture of water-glycerin at 80% in weight in contact with air, based on the experimental conditions of Thoraval *et al.* [20]; (B) a mixture of water-glycerin at 50% in weight in contact with air. The respective physical properties are listed in Table I. We also restrict our work to vertical planes.

All simulations have a computational domain of size $0.1 \times 0.01 \times 0.08$ m (length L, height H, and width W with reference to Fig. 1), except for the simulations where the inlet width has been varied (here, $W = 0.1$ m to allow us to employ a larger range of liquid inlet, and $H = 0.006$ m). Indeed, we vary the width ℓ_z of the liquid inlet such that it remains always shorter than the computational domain width (Fig. 1), to avoid any interaction of the liquid with the borders.

The control parameters of the problem and their range of variations are shown in Table II. In addition to the inclination angle β and the contact angle θ_s, the other dimensionless control parameters are the Reynolds, capillary, and Bond numbers, as well as the width-to-height ratio ℓ_z/h_0, where ℓ_z is the inlet width and h_0 the inlet film thickness.

The liquid Reynolds number Re_l is based on the volumetric flow rate per unit width $q = Q/\ell_z$, where Q is the volumetric flow rate:

$$\mathrm{Re}_l = \frac{q}{\nu_l} = \frac{U_0\, h_0}{\nu_l}, \tag{10}$$

where U_0 and h_0 correspond to the velocity and thickness of the Nusselt flat (waveless) film (Nusselt [34]), for which

$$U_0 = \frac{g \sin\beta\, h_0^2}{3\, \nu_l}. \tag{11}$$

Indeed, behind the advancing rim there is a portion of flat (waveless) film, whose thickness and velocity are consistent with the Nusselt equilibrium condition. The capillary number Ca is

TABLE II. Control parameters and their range of variations of the numerical study. Top: dimensional parameters, bottom: dimensionless parameters.

Control parameter	Notation	Range of variation
Film thickness	h_0	(0.60–1.76) mm
Film velocity	U_0	(0.05–0.55 m/s
Liquid inlet width	ℓ_z	(0.04–0.098) m
Inclination angle	β	90°
Contact angle	θ_s	40°–160°
Liquid Reynolds number	Re_l	1.2–101
Capillary number	Ca	0.019–0.188
Bond number	Bo	0.06–0.56
Width-to-height ratio	ℓ_z/h_0	49–121

defined as

$$\mathrm{Ca} = \frac{\mu_l\, U_0}{\gamma}, \tag{12}$$

whereas the Bond number as

$$\mathrm{Bo} = \frac{\rho_l\, g\, h_0}{\gamma}. \tag{13}$$

The boundary conditions applied at the inlet replicate the presence of an opening where the working liquid falls from. Those can be expressed as

$$u(0, y, z) = U_0 \quad \text{if} \quad y \leqslant h_0 \qquad \text{and} \qquad u(0, y, z) = 0 \quad \text{if} \quad y > h_0. \tag{14}$$

With reference to Fig. 1, at the left, right, top, and bottom boundaries, the applied conditions are

$$u(x, 0, z) = u(x, H, z) = 0, \tag{15}$$

$$u(x, y, 0) = u(x, y, W) = 0, \tag{16}$$

except for the simulations of Sec. III A, where at the top boundary a symmetry condition is instead imposed. At the outlet, a Neumann condition is imposed for the volume fraction and for the pressure:

$$\nabla\varphi(L, y, z) = 0, \tag{17}$$

$$\frac{\partial^2 p}{\partial x\, \partial y}(L, y, z) = 0. \tag{18}$$

The Neumann condition for the pressure is imposed in a single outlet point (L, y_0, z_0) with reference pressure p_0, and then the pressure field at the outlet is obtained through an iterative method based on the values of the pressure in the neighbor cells.

As initial condition, a liquid step is imposed adjacent to the inlet, whose size matches a few grid points in the streamwise direction, h_0 in the cross-stream direction and ℓ_z in the spanwise direction. Within the step, the velocity is consistent with the liquid inlet, i.e., $u = U_0$. The imposed initial velocity is otherwise zero.

A thorough validation of the numerical code JADIM in the film spreading scenario is discussed in the Appendix.

III. RIVULET CASCADE AND EXPLANATION OF THE INSTABILITY MECHANISM

A. Rivulet cascade

We now focus on the time evolution of a liquid film of partially wetting fluid falling down a vertical wall with side contact lines. The problem is similar to the one studied by Lan *et al.* [19], except that the liquid Reynolds number is now significantly smaller and the wall is more hydrophobic. The flow conditions considered here are fluid A, $\mathrm{Re}_l = 2.92$, $\mathrm{Ca} = 0.04$, $\theta_s = 82.5^\circ$. This set of flow conditions leads to a completely different flow pattern with respect to Lan *et al.* [19], with formation of rivulets.

In order to investigate the behavior of the advancing contact line in time, we consider three different inlet widths: $\ell_z/h_0 = (55.6, 105.1, 121.2)$ corresponding to $\ell_z = (0.45, 0.85, 0.98)$ of the entire domain width $W = 0.1$ m. Figure 2 shows snapshots of the falling film and of the rivulet dynamics, by computing the contour level $\varphi = 0.5$ of the volume fraction. In order to highlight the 3D effects of this complex dynamics, we use contrast between the 3D image and a grid pattern in the background. Time is rendered dimensionless as $t^\star = t\, U_0/h_0$. At early stages, in all the considered cases, two symmetric fingers appear at the side contact line (leftmost panels). These fingers travel faster than the flat (waveless) film in between. Meanwhile, the film width decreases (second panels from the left). Subsequently, the flat (waveless) film between the initial lateral rivulets destabilizes

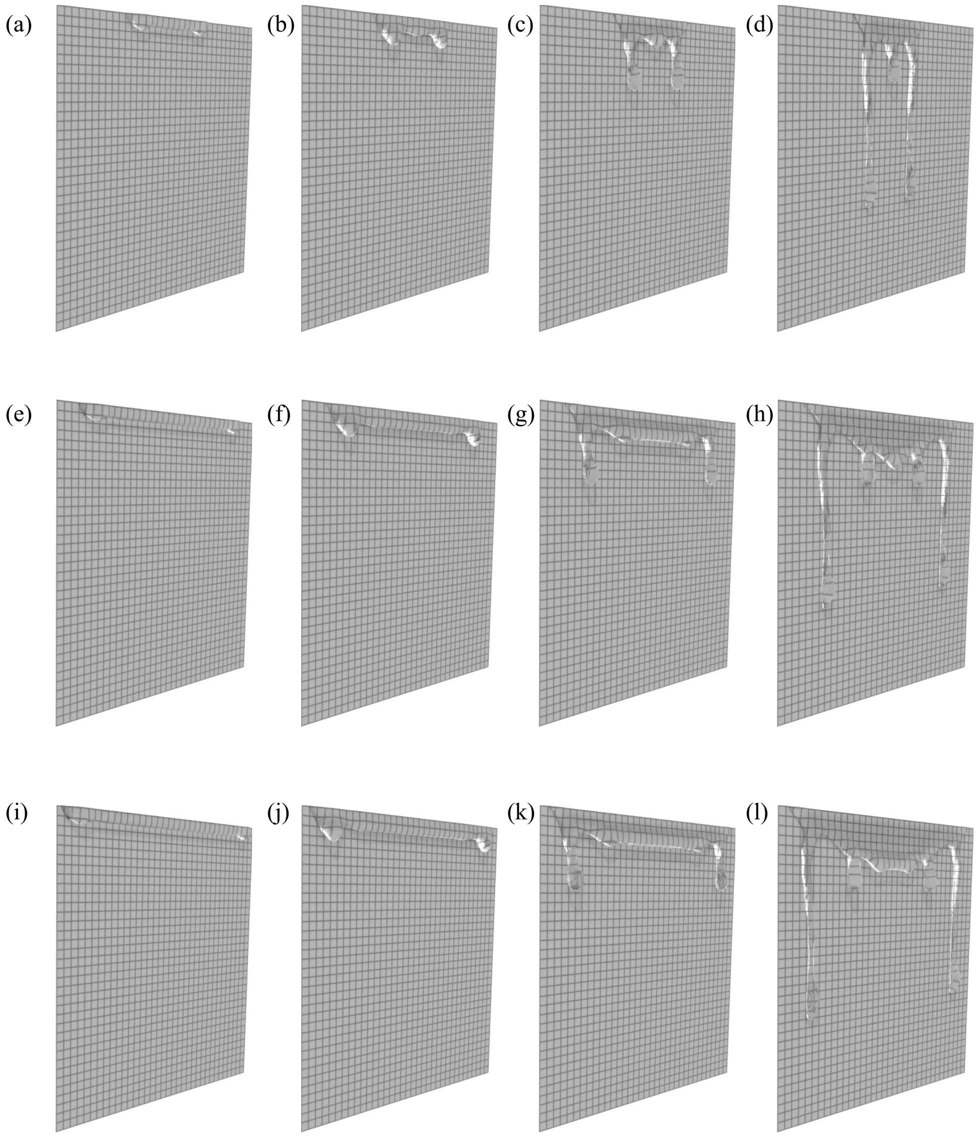

FIG. 2. Snapshots of 3D view of a liquid film of fluid A down a vertical plane at $\mathrm{Re}_l = 2.92$, $\mathrm{Ca} = 0.04$, $\theta_s = 82.5^\circ$. (a)–(d): $\ell_z/h_0 = 55.6$, i.e., $\ell_z/W = 0.45$; (e)–(h): $\ell_z/h_0 = 105.1$, i.e., $\ell_z/W = 0.85$; (i)-(l): $\ell_z/h_0 = 121.2$, i.e., $\ell_z/W = 0.98$. Time steps: $t^\star = 9.78$ (leftmost panels); $t^\star = 16.3$ (second panels from the left); $t^\star = 22.8$ (third panels from the left); $t^\star = 29.3$ (rightmost panels).

and additional fingers originate (third panels from the left). In the first case, where $\ell_z/W = 0.45$, only one extra rivulet appears, while in the second case ($\ell_z/W = 0.85$) the new forming rivulets are in the number of two. If the inlet width is further increased, as in the third case ($\ell_z/W = 0.98$), the number of new rivulets does not change. If the distance between the last formed couple of rivulets is large enough, a cascade takes place in the form of a series of twin rivulets (rightmost panels). This is a self-sustained rivulet cascade from the side to the center.

We now turn to the analysis of rivulet length and unstable wavelength throughout the cascade. Lines with empty symbols in Fig. 3(a) show the rivulet length in time for the configuration with

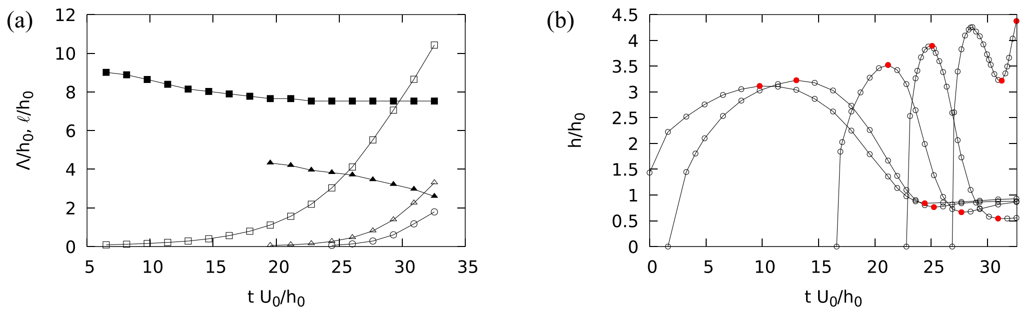

FIG. 3. Time evolution of finger dynamics for the case $\ell_z/W = 0.85$ [Figs. 2(e)–2(h)]. (a) Length of main rivulets ℓ_I (empty square), secondary rivulets ℓ_{II} (empty triangle), and tertiary rivulets ℓ_{III} (empty circle). Wavelength of main rivulets Λ_I (filled square) and secondary rivulets Λ_{II} (filled triangle). (b) Rim profile at the spanwise center at different streamwise positions, from left to right: $x/L = 0.001, 0.02, 0.06, 0.1, 0.15$. Filled red circles mark the position of maximum and minimum film thicknesses.

$\ell_z/W = 0.85$. The first couple of rivulets (square) accelerates and then reach a constant velocity value, almost when the second couple (triangle) and the last (central) finger (circle) appear. The time evolution of all three flow structures is similar but shifted. Lines with filled symbol represent the distance between the twin rivulets forming the first (square) and the second (triangle) couple. This distance decreases at initial stages. This behavior is explained by the pattern depicted in the rightmost panels of Fig. 2, where the two lateral rivulets diverge next to their roots. However, when the rivulet velocity reaches a constant value, the distance no longer varies.

Figure 3(b) shows the time evolution of the film thickness profile at the center of the domain ($z/W = 0.5$) for different streamwise positions. As expected, the ridge becomes thicker and narrower as it flows down the plane driven by gravity. This is shown by the red filled circles, which mark the position of maximum and minimum film thicknesses for each streamwise position. The capillary ridge anticipates the passage of the waveless film, whose thickness corresponds to the Nusselt value. Small deviation from this limit should be expected due to the presence of an active gas phase, which exerts a shear stress on the liquid film and thus modifies the velocity profile within the liquid (Lavalle *et al.* [35]). The rightmost line shows the film thickness profile when the capillary ridge destabilizes into the central finger.

1. Influence of inertial effects and film thickness effects

In this section, we investigate the effect of the Reynolds number on the overall finger pattern. However, varying the Reynolds number entails the variation of the film thickness too, as Re_l and h_0 are linked through the Nusselt equilibrium condition (10) and (11).

In order to decouple the inertial effects from the film thickness effects, we have employed another working liquid (fluid B of Table I). Using fluid A and fluid B allows us to maintain the film thickness fixed while varying the Reynolds number and vice versa.

First, we consider the configurations depicted in Figs. 4(a) and 4(c). Here, while the film thickness is unchanged, the Reynolds number varies from 1.2 to 28.3 by changing the working liquid [fluid A for Fig. 4(a) and fluid B for Fig. 4(c)], while keeping almost constant the capillary and the Bond numbers.

From Figs. 4(a) and 4(c), the inertial effects strongly influence the general flow pattern, although the average wavelength is similar. Particularly, the decrease in film width is less pronounced for $\mathrm{Re}_l = 28.3$ [Fig. 4(c)], as also observed by Lan *et al.* [19]. Indeed, the film restriction is governed by the competition of surface tension effects, which tend to center the film, against inertial effects and weight of the lateral rim, which promote the film stretching.

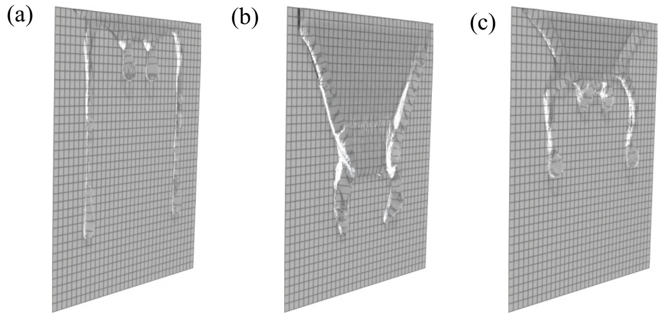

FIG. 4. 3D view of a liquid film down a vertical plate. (a) Fluid A: $\mathrm{Re}_l = 1.2$, $h_0 = 0.60$ mm, $\ell_z/h_0 = 116.7$, $t^\star = 29.3$. (b) Fluid A: $\mathrm{Re}_l = 30$, $h_0 = 1.76$ mm, $\ell_z/h_0 = 39.8$, $t^\star = 29.3$. (c) Fluid B: $\mathrm{Re}_l = 28.3$, $h_0 = 0.60$ mm, $\ell_z/h_0 = 116.7$, $t^\star = 75.8$.

Comparing Figs. 4(b) and 4(c) allows us to analyze the film thickness effects. Here, while the Reynolds number is almost unchanged, the film thickness is different due to the change of working liquid [fluid A for Fig. 4(b) and fluid B for Fig. 4(c)]. We observe that the film thickness effects also play on the overall finger pattern. The decrease in film width is weaker at high film thickness [Fig. 4(b)]. This is due to the greater thickness of the lateral rim, which fosters the film stretching together with inertia, against surface tension effects. The configuration at high h_0 [Fig. 4(b)] exhibits another interesting feature: only the lateral rivulets develop, as the twin central rivulets are overwhelmed by the displacement of the waveless film behind the front contact line.

B. Mechanism for width restriction and rivulet cascade

Figure 4(c) clearly shows the presence of two characteristic regions in the falling film: (i) The uniform (waveless) film behind the front contact line, which flows in the direction of gravity. Here, the viscous stresses balance the weight of the film, and their resulting balance leads to the Nusselt velocity profile (11). (ii) The lateral rim, which forms due to the film restriction, and which collects the liquid from the upcoming flow. We analyze the equilibrium of the lateral rim in the direction *perpendicular* to the contact line, governed by the balance of capillary forces, which tend to promote the width restriction, and of gravity (i.e., rim weight) and momentum flux carried by the uniform film, which both tend to keep the film straight and the lateral rim vertical. Since the velocity U_{cl} of the lateral contact line is very low, we can suppose that the viscous stresses do not play in the equilibrium of the rim along the direction perpendicular to the lateral contact line. We have verified this for two limit cases ($\mathrm{Re} = 1.2$ and $\mathrm{Re} = 30$) by quantifying the gravity term ($\rho g \sin \psi$, where ψ is the angle between the side contact line and the vertical; see Fig. 5) with respect to the viscous drag in the direction normal to the contact line ($\mu U_{cl}/h_{\mathrm{rim}}^2$, where h_{rim} is the thickness of the lateral rim). This ratio can be formulated in terms of the dimensionless group $\mathrm{Bo}_{\mathrm{rim}} \sin \psi / \mathrm{Ca}_{cl}$, where

$$\mathrm{Bo}_{\mathrm{rim}} = \rho_l g h_{\mathrm{rim}}^2 \gamma^{-1} \tag{19}$$

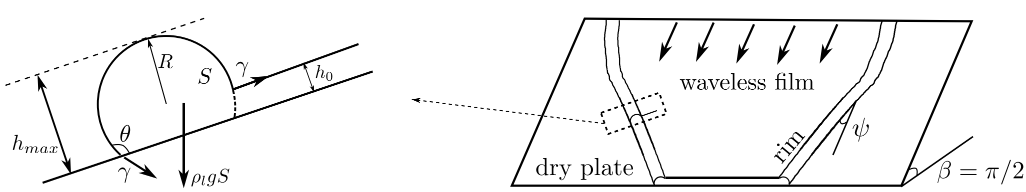

FIG. 5. Sketch of a falling film with side contact lines and of the lateral rim (zoomed area).

is the Bond number based on $h_{\rm rim}$. Given that $\mathrm{Bo}_{\rm rim}\sin\psi/\mathrm{Ca}_{cl}$ is much larger than unity ($\mathrm{Bo}_{\rm rim}\sin\psi/\mathrm{Ca}_{cl}\simeq 20$ for the scenario $\mathrm{Re}=1.2$, and $\mathrm{Bo}_{\rm rim}\sin\psi/\mathrm{Ca}_{cl}\simeq 8$ for the scenario $\mathrm{Re}=30$), the viscous stresses in the direction perpendicular to the lateral contact line are much smaller than the rim weight.

To identify the mechanism responsible for the width restriction, we consider the balance of forces acting on the rim along the normal direction to the side contact line (Fig. 5). Following Sebilleau *et al.* [36], the balance of forces reads

$$\gamma(1-\cos\theta)=\rho_l g S\sin\psi+\frac{2}{15}\frac{\rho_l g^2 h_0^5}{\nu_l^2}\sin\psi^2, \tag{20}$$

where S is the surface of the rim (Fig. 5). The rim surface S can be expressed as the area of a circular segment, i.e., $S=R^2(\theta-\sin\theta\cos\theta)$. Here, R is the radius of curvature of the rim, which is related to the maximum rim height $h_{\rm rim}$ through the relation

$$h_{\rm rim}=R(1-\cos\theta), \tag{21}$$

under the assumption that the rim shape can be approximated by a circular segment (Fig. 5). Equations (20) and (21) hold for all contact angles: $0\leqslant\theta\leqslant\pi$.

In dimensionless form, and by expressing S and R as a function of θ, the balance of forces (20) reads

$$(1-\cos\theta)=\mathrm{Bo}_{\rm rim}\frac{\theta-\sin\theta\cos\theta}{(1-\cos\theta)^2}\sin\psi+\frac{2}{5}\mathrm{Re\,Bo}\sin\psi^2. \tag{22}$$

Equation (22) can be solved in ψ as a function of Re Bo. However, neither $\mathrm{Bo}_{\rm rim}$ nor θ are known. It turns out that the rim height $h_{\rm rim}$ is roughly uniform along the streamwise direction. For all simulated cases with $\theta=82.5^\circ$, we have $h_{\rm rim}/h_0\simeq 2$ for fluid A whereas $h_{\rm rim}/h_0\simeq 2.5$ for fluid B, which allows us to express $\mathrm{Bo}_{\rm rim}$ as a function of Bo. The contact angle θ in Eq. (22) must be computed by employing the dynamic contact angle model (8). For this, the capillary number Ca_{cl} based on the lateral contact-line velocity U_{cl} must be evaluated. Two regimes are identified: (i) Static lateral contact line, for which $\mathrm{Ca}_{cl}\simeq 0$. This is the case of fluid B. (ii) Dynamic lateral contact line, for which Ca_{cl} can be evaluated by fitting the DNS data. This is the case of fluid A.

Before fitting the DNS data, we attempt to find the relation between Ca_{cl} and Re Bo. When Re Bo is large (>20), Eq. (22) mainly gives the equilibrium between the capillary term and the momentum carried by the film:

$$(1-\cos\theta)\simeq\frac{2}{5}\mathrm{Re\,Bo}\sin\psi^2. \tag{23}$$

From the inset shown in Fig. 6(b), we recover that $\sin\psi^2\sim(\mathrm{Re\,Bo})^{-2/3}$. As a consequence, for $\theta\to\pi$ (the dynamic angle $\theta>150^\circ$ in our cases), Eq. (23) simplifies to

$$\theta^2\sim(\mathrm{Re\,Bo})^{1/3}. \tag{24}$$

By using the Cox-Voinov model (8) to express θ, and by neglecting, as a first approximation, θ_s with respect to the term in Ca_{cl} (this is a valid approximation for large Re Bo), one obtains

$$\mathrm{Ca}_{cl}^{2/3}\sim(\mathrm{Re\,Bo})^{1/3}, \tag{25}$$

which leads to the relation $\mathrm{Ca}_{cl}\sim(\mathrm{Re\,Bo})^{1/2}$.

We have verified that the curve that fitted best with the DNS points yielded a dependence of the form

$$\mathrm{Ca}_{cl}=0.04\sqrt{\mathrm{Re\,Bo}}-0.025. \tag{26}$$

This is represented in Fig. 6(a), which also shows the variation of Ca (based on the undisturbed film velocity U_0) as a function of Re Bo (dashed line). This scales as $(\mathrm{Re\,Bo})^{2/5}$ given that $\mathrm{Ca}\sim h_0^2$ and $\mathrm{Re}\sim h_0^3$ [Eqs. (10) and (11)]. Therefore, $\mathrm{Ca}/\mathrm{Ca}_{cl}\sim(\mathrm{Re\,Bo})^{-1/10}$.

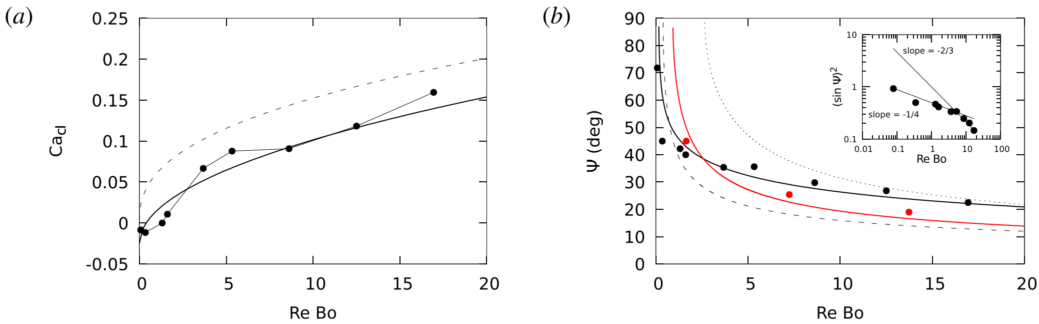

FIG. 6. (a) Capillary number based on the contact-line velocity as a function of Re Bo: DNS results (circle); fit curve: $0.04\sqrt{\mathrm{Re\,Bo}} - 0.025$ (solid thick line). Dashed line: capillary number based on U_0. (b) Angle ψ made by the decrease in film width in a falling film of partially wetting fluid ($\theta_s = 82.5°$) as a function of Re Bo, obtained via Eq. (22) (black solid line: fluid A; red solid line: fluid B). Filled circles mark the DNS results (black: fluid A; red: fluid B). The dashed line indicates the viscous-capillary limit [Eq. (22) without inertial term and with $\theta = \theta_s$] whereas the dotted line the purely inertial limit [Eq. (22) with $\mathrm{Ca}_{cl} = \mathrm{Ca}$]. Inset shows the log-log plot of $\sin\psi^2$ as a function of Re Bo for fluid A.

By employing the relation (26) into the dynamic model (8) for fluid A, and $\mathrm{Ca}_{cl} = 0$ for fluid B, Eq. (22) can be finally solved numerically. The variation of ψ as a function of Re Bo is shown in Fig. 6(b). The agreement between the model (22) (solid lines) and the corresponding DNS results (filled circles) for fluid A (black) and fluid B (red) is good for all values of Re Bo. In the same graph, we have also represented two additional curves for fluid A: (i) the inertia-dominated regime, obtained by solving Eq. (22) by employing Ca in the Cox-Voinov model (8), as if the side contact line advances with U_0 (dotted line); (ii) the purely capillary/viscous regime, obtained by solving Eq. (22) without the inertial term, in line with Podgorski *et al.* [37], and by employing $\theta = \theta_s$ (dashed line). We note that the latter captures the decrease in film width only for small values of Re Bo, whereas the purely inertial model works well only for large values of Re Bo. Thus, employing the contact-line model (26) into the Cox-Voinov model (8) allows us to correctly predict the decrease in film width ψ for all Re Bo.

Finally, the inset in Fig. 6(b) shows that $\sin\psi^2$ scales as $\mathrm{Re\,Bo}^{-2/3}$ at large Re Bo. As described earlier, this dependence justifies the use of the relation (26).

The combination of width restriction and mass conservation induces the acceleration of liquid towards the center. This is responsible for the formation of the first couple of rivulets on the sides, which initiates the cascade. Figure 7 shows this mechanism into play, by representing snapshots of velocity magnitude field [Figs. 7(a)–7(c)] and spanwise velocity field [Figs. 7(d)–7(f)] for the scenario with $\ell_z/W = 0.85$ [Figs. 2(e)–2(h)]. Figures 7(a) and 7(d) show the two lateral fingers forming due to the acceleration of liquid in the spanwise direction. At this stage, the cascade takes place as follows (for simplicity we describe only the left half of the domain): further to the development of the first lateral finger, the liquid is prone to flow therein. This is shown, for instance, in Fig. 7(d), where a blue region forms next to the red one and grows in intensity with time [Fig. 7(e)]. Then, a new region of opposite spanwise velocity (red) takes place, as shown in Fig. 7(f). Meanwhile, a stagnation zone forms next to the lateral fingers [white area in Figs. 7(a)–7(c)]. This creates regions of different velocity at the front contact line which is the basic mechanism for the formation of additional fingers [3,16], thus feeding the cascade.

We now identify the role of the spanwise velocity in the destabilization of the first couple of rivulets. For the scenario with $\ell_z/W = 0.85$ [Figs. 2(e)–2(h)], we evaluate the Young-Laplace equation at two representative spanwise positions, e.g., at the center of the domain ($z/W = 0.5$) and

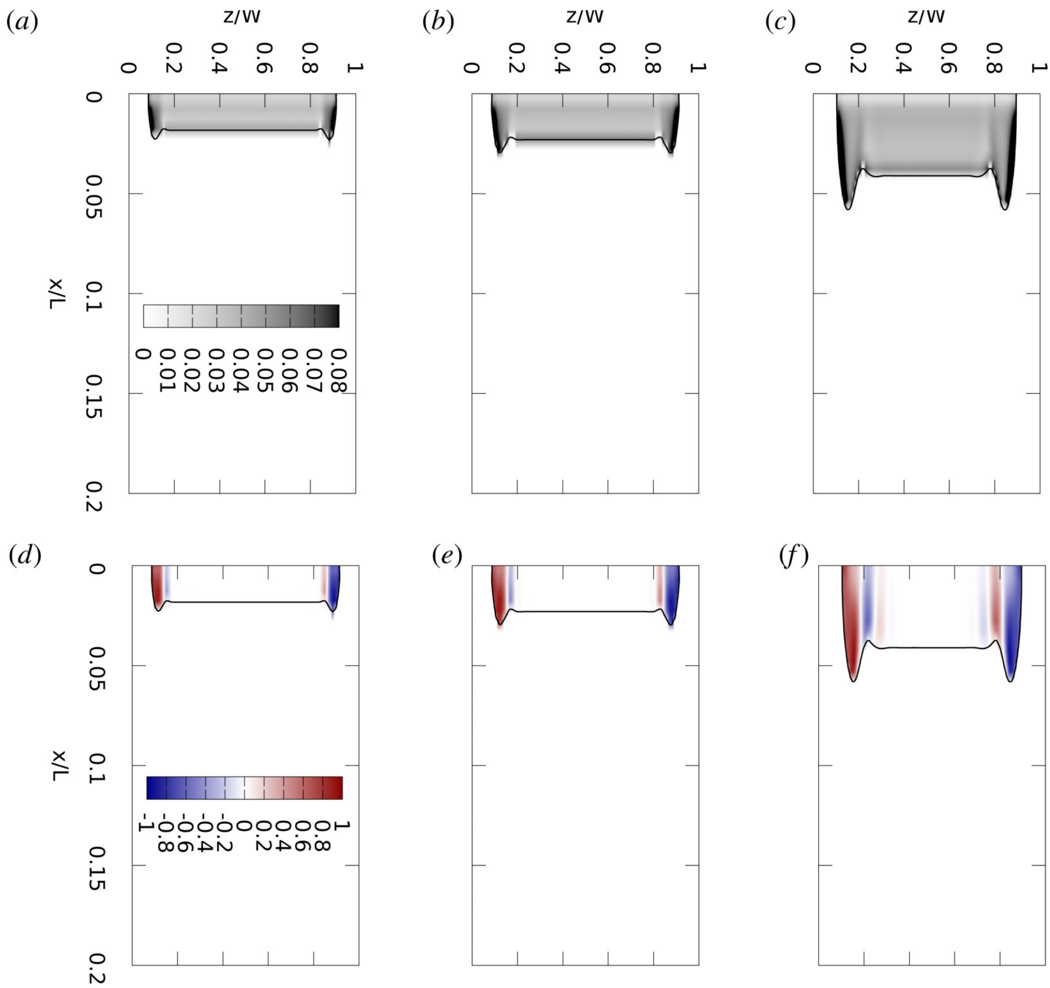

FIG. 7. Top view of a liquid film of fluid A down a vertical plate at $\mathrm{Re}_l = 2.92$, $\theta_s = 82.5^\circ$, and $\ell_z/W = 0.85$ [same case as Figs. 2(e)–2(h)]. Snapshots of the velocity field along the plane xz. (a)–(c): Module of velocity. (d)–(f): Normalized spanwise velocity.

next to the border ($z/W = 0.905$), as shown by vertical dashed lines in Fig. 8:

$$p_l - p_g = \frac{\gamma}{R}, \tag{27}$$

where R is the radius of curvature given by Eq. (21). 3D effects are negligible even at the border representative position.

Figure 8(a) represents the pressure field along a yz plane next to the inlet ($x/L = 0.008$). The pressure is greater at the border (index b) than at the midpoint (index c) position, for which $R|_b < R|_c$ following Eq. (27). Given that $\theta|_b \simeq \theta|_c$, as depicted in the two insets of Fig. 8(a) (where tics correspond to 0.5 mm), it follows from Eq. (21) that $h_{\max}|_b < h_{\max}|_c$, which is clearly not the case. This inconsistency suggests that the spanwise velocity within the film plays a role here. This is confirmed by the analysis of dimensionless numbers, for which $We = \rho_l U_0^2 h_0 \gamma^{-1} = 0.12$ while $\mathrm{Ca} = 0.04$. By including inertia effects into the Eq. (27) one obtains

$$p_l - p_g = \frac{\gamma}{R} + \frac{1}{2}\rho_l u^2. \tag{28}$$

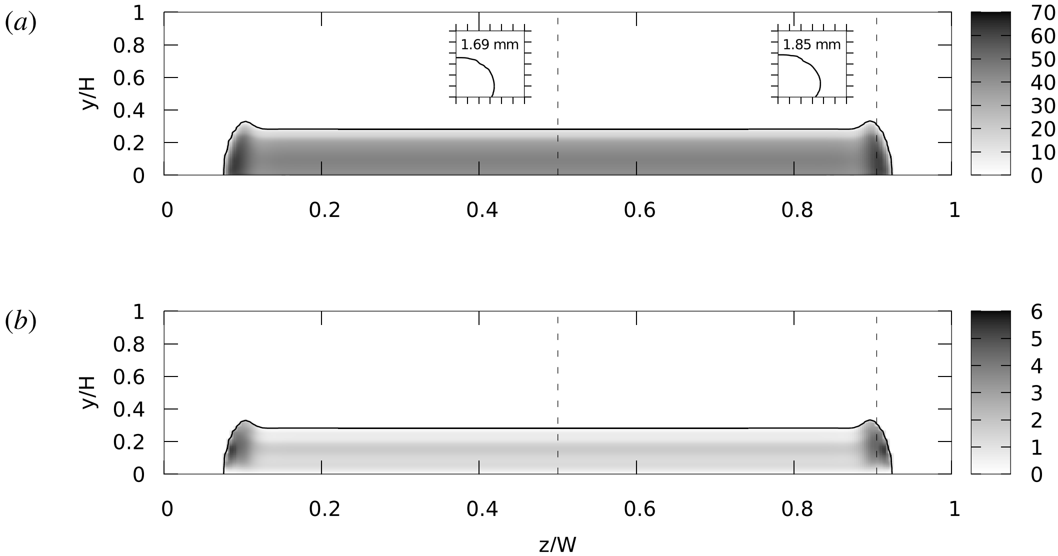

FIG. 8. Front view (at the position $x/L = 0.008$) of a liquid film of fluid A down a vertical plate at $\mathrm{Re}_l = 2.92$, $\theta_s = 82.5^\circ$, and $\ell_z/W = 0.85$ [Figs. 2(e)–2(h)] at $t^\star = 1.63$. (a) Pressure field. (b) Field of $1/2\rho_l u^2$. Insets show the film thickness profile and $h_{\max}$ at the spanwise positions identified by dashed lines. The abscissa has been compressed by 3.4 times for visibility purposes.

The dynamic contribution $1/2\rho_l u^2$ to the pressure is represented in Fig. 8(b). The effect of the liquid acceleration at the border makes the term γ/R smaller, and thus $h_{\max}$ greater. For instance, at the border we have $p_l - p_g = 62$ Pa, $\theta = 125^\circ$, and $1/2\rho_l u^2 = 4.44$ Pa. The analysis of these data gives $h_{\max} = 1.62$ mm from Eq. (27) and $h_{\max} = 1.75$ mm from Eq. (28), which is closer to the numerical value 1.85 mm shown in the inset of Fig. 8. We may thus conclude that the velocity at the border (and particularly the spanwise component w) within the film plays a great role for the lateral destabilization.

IV. WAVELENGTH SELECTION

We now study how the general topology of the flow changes with inlet width, contact-line perturbations, and contact angle. For this, we employ the fluid A for its richer dynamics, as the dynamic contribution to the contact angle is not negligible (Sec. III B). We are particularly interested in number and length of the observed rivulets, as well as in the wavelength selection with respect to the prediction of linear stability. Specifically, we compare the average distance between the rivulets resulting from our simulations to the linear stability results obtained via the lubrication approximation [16,38].

According to this, the most unstable wavelength $\lambda_{\max}$ is defined as

$$\lambda_{\max} = \kappa \frac{h_0}{(3\mathrm{Ca})^{1/3}}, \tag{29}$$

where κ is a constant which was determined experimentally by Johnson *et al.* [8] ($\kappa = 13.9$), by Silvi and Dussan [5] ($\kappa = 17$), by Huppert [4] ($\kappa = 18$), and through linear stability analysis under the lubrication approximation by Troian *et al.* [38] and by Kondic and Diez [16] ($\kappa = 14$). By way of linear stability analysis in the lubrication approximation one can also recover the cutoff wavelength

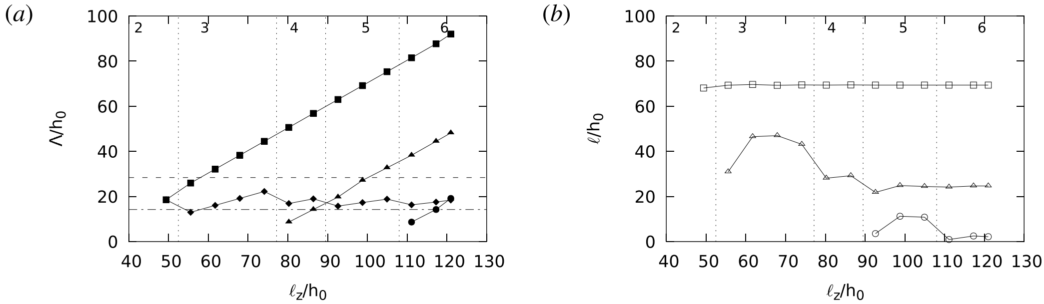

FIG. 9. Effect of width-to-height ratio ℓ_z/h_0 at $t = 0.27$ s ($t^\star = 29.3$) on the finger dynamics of a film of fluid A flowing vertically at $\mathrm{Re}_l = 2.92$, $\mathrm{Ca} = 0.04$, with $\theta_s = 82.5°$. (a) Dimensionless primary wavelength Λ_I/h_0 (filled square), secondary wavelength Λ_{II}/h_0 (filled triangle), tertiary wavelength Λ_{III}/h_0 (filled circle), average wavelength $\bar{\Lambda}$ (filled diamond). The horizontal lines mark the most unstable wavelength (dashed line) and cutoff wavelength (dash-dotted line) from linear theory (Troian *et al.* [38]). (b) Dimensionless primary rivulet length ℓ_I/L (empty square), secondary rivulet length ℓ_{II}/ℓ_I (empty triangle), tertiary rivulet length ℓ_{III}/ℓ_I (empty circle). The number at the top of each graph indicates the number of observed rivulet whereas the vertical dotted lines mark their threshold.

(the shortest unstable wavelength) as

$$\lambda_c = \omega \frac{h_0}{(3\mathrm{Ca})^{1/3}}, \tag{30}$$

where $\omega = 7$ for Troian *et al.* [38] and $\omega = 8$ for Kondic and Diez [16]. However, we emphasize that Eqs. (29) and (30) are obtained by solving the linear stability problem based on the long-wave approximation, whereas the numerical simulations employed in this work make use of the full Navier-Stokes equations.

A. Influence of varying the inlet width

We start by investigating the effect of varying the width-to-height ratio ℓ_z/h_0 by varying ℓ_z. The liquid inlet width has been varied in the range $\ell_z/W = (0.4–0.98)$, thus $\ell_z/h_0 = (49.4–121.2)$. All other control parameters remain unchanged: fluid A, $\mathrm{Re}_l = 2.92$, $\mathrm{Ca} = 0.04$, $\beta = 90°$, $\theta_s = 82.5°$.

Figure 9 shows the effect of the inlet width on rivulet length and distance at a given time ($t^\star = 29.3$). The case $\ell_z/h_0 = (55.6, 105.1, 121.2)$ corresponds to the scenario depicted in the rightmost panels of Fig. 2.

In Fig. 9(a) the primary wavelength Λ_I, i.e., the tip-to-tip distance between the first-forming rivulets, grows linearly with the inlet width (filled square). In fact, the decrease in film width is unchanged when varying the inlet width; thus the lateral rivulet distance follows the variation of the inlet. For sufficiently wide liquid inlet ($\ell_z/W \geqslant 0.65$), a couple of central rivulets form as a result of the cascade development, as described in the previous section. Their wavelength Λ_{II} also increases linearly with the inlet width (filled triangle) with a similar slope as Λ_I. A further increase of the inlet width ($\ell_z/W \geqslant 0.9$) leads to the formation of a new couple of central rivulets, whose wavelength Λ_{III} again increases with the same behavior (filled circle). The final number of observed rivulets is specified by the number at the top of the graph.

In order to compare the wavelength selection with the prediction of linear instability, we have also represented the most unstable (dashed line) and the cutoff (dash-dotted line) wavelength from linear theory (Troian *et al.* [38]), i.e., Eqs. (29) and (30). It turns out that the average distance between the observed fingers (filled diamond) falls within the unstable branch predicted by the linear instability for all the simulated cases.

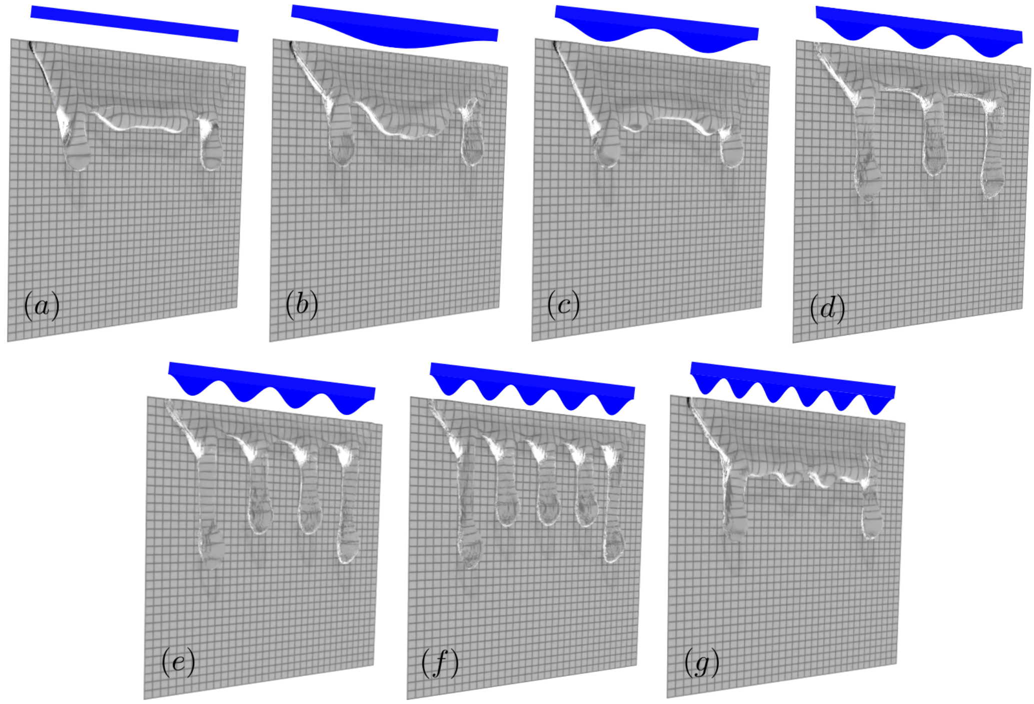

FIG. 10. 3D view of the flow dynamics at $t^\star = 22$ of a vertical film of fluid A with $\mathrm{Re}_l = 7.3$, $\mathrm{Ca} = 0.07$, $\theta_s = 82^\circ$, and $\ell_z/h_0 = 63.6$. Effect of the contact-line perturbation $\epsilon \cos(2\pi\, k\, z/\ell_z)$: $k = 0$ (a); $k = 1$ (b); $k = 2$ (c); $k = 3$ (d); $k = 4$ (e); $k = 5$ (f); $k = 6$ (g).

In Fig. 9(b), the length of the first (square), second (triangle), and third (circle) couple of rivulets is shown as a function of the inlet width at a given time. While the length of the first couple of rivulets is unaltered, the length of the second and third couple is slightly modified by the inlet width variation.

B. Influence of contact-line shape perturbations

We now study the role of contact-line shape perturbations on the general flow dynamics. We aim at investigating whether the wavelength selection is modified by the initial perturbation of the contact line. For a perturbation composed of more than one mode, which would model the noise of an experiment, the observed pattern follows the most unstable wavelength [10]. In this section, we instead apply a single-mode sinusoidal perturbation and compare the resulting wavelength to linear stability predictions. The application of a single-mode perturbation can also be achieved experimentally, as in Lerisson *et al.* [39] for inverted falling films.

For all simulated cases, we have fluid A, $\mathrm{Re}_l = 7.3$, $\mathrm{Ca} = 0.07$, $\theta_s = 82^\circ$, and $\ell_z/h_0 = 63.6$. In this scenario, the most unstable wavelength predicted by linear stability analysis is $\lambda_{\max} = 25.5$ mm from Eq. (29), whereas the cutoff wavelength is $\lambda_c = 12.3$ mm from Eq. (30). Given that the width of the inlet gap is $\ell_z = 0.07$ m (7/8 of the entire domain width), it turns out that the liquid inlet is comparable to the typical pattern distance, $\ell_z/\lambda_{\max} = 2.75$.

We distinguish eight types of initial conditions by forcing the contact line with a single-mode perturbation of the form $\epsilon \cos(2\pi\, k\, z/\ell_z)$, where $\epsilon = 0.9\, h_0$ is the amplitude and $k = (0, 6)$. The eighth type of initial condition is obtained by applying a phase shift at the configuration with $k = 4$, i.e., $\epsilon \cos(8\pi\, z/\ell_z + \chi)$ with $\chi = \pi/2$.

TABLE III. Rivulet number n and ratio of the imposed wavelength $\lambda_i = \ell_z/k$ to $\lambda_{\max}$ and λ_c.

k	n/k	$\lambda_i/\lambda_{\max}$	λ_i/λ_c
0		2.75	5.5
1	2	2.75	5.5
2	1	1.37	2.75
3	1	0.92	1.83
4	1	0.69	1.37
5	1	0.55	1.1
6	0.67	0.46	0.92

We start by discussing the seven configurations without phase shift. Figure 10 shows the 3D flow dynamics for the perturbations corresponding to $k = (0, 6)$. Three regimes are identified depending on the imposed wavelength $\lambda_i = \ell_z/k$ (see also Table III): (i) When $\lambda_c < \lambda_i < \lambda_{\max}$ [Figs. 10(d)–10(f)], the number of rivulets is consistent with the initial perturbation, as roots and tips are in phase with the contact-line perturbation, represented in blue at the top of each panel. Therefore, when the perturbation wavelength is shorter than the most unstable wavelength $\lambda_{\max}$ (scenarios $k = 4$ and $k = 5$), the system does not select the wavelength λ_m, or a combination of λ_m and λ_i, but simply follows the perturbation. (ii) When $\lambda_i < \lambda_c$ [Fig. 10(g)], the perturbation wavelength is shorter than the cutoff wavelength λ_c. As a result, the system no longer follows the initial condition and evolves in a state with two central rivulets and two longer rivulets on the sides. (iii) When $\lambda > \lambda_{\max}$ [Figs. 10(a)–10(c)], the pattern is characterized by the formation of two lateral rivulets and a central advancing ridge. These results are summarized in Table III. We can thus conclude that despite the perturbation of the contact line, the two lateral rivulets always develop first, then the others. Interestingly, when the perturbation wavelength is slightly larger than λ_c, the rivulet cascade is suppressed, in the sense that all the central rivulets form at the same time and progress simultaneously [Fig. 10(f)].

Among the scenarios with varying spanwise wave number perturbations, we now identify the case where the amplification of the contact-line instability is the greatest. For this, Fig. 11(a) shows the spatial growth rate, defined as the maximum film thickness at a given position (x_0, z_0) in time: $h_{\max} = \max[h(x_0, z_0, t)]$, where z_0 always coincides with the initial perturbation tip closer to the center of the domain. The inset shows how the maximum is computed: for a given z_0, x_0 is varied as $x_0/L = j\,0.01\,x/L$, with $j = (0, 10)$; for each x_0, $h_{\max}$ corresponds to the maximum film thickness in time. Precisely, the inset shows the maximum film thickness at the positions $x/L = 0.05$ and $x/L = 0.1$ for the case $k = 4$. The configurations with the maximum growth rate are those with $k = 3$ (up-pointing triangle) and $k = 4$ (down-pointing triangle), for which the perturbation wavelength λ_i is closer to $\lambda_{\max}$ (see third column of Table III). Also, the scenario with $k = 6$ (cross) for which $\lambda_i < \lambda_c$ (fourth column of Table III) has a small growth rate. However, the case without perturbation (plus) is the one with the weakest growth rate, suggesting that perturbing the contact line has a beneficial effect regardless of the perturbation wavelength.

Further, we are interested in identifying the contact-line perturbation that is more inclined to promote the best plate covering. For this, we evaluate the root velocity of the lateral rivulets by representing the root length ℓ_r in time (see Fig. 1 for the definition of ℓ_r). Figure 11(b) shows that the growth of ℓ_r is exponential in time until $t^\star = 22$. This is the time chosen for representing the 3D pattern in Fig. 10. The inset of Fig. 11(b) shows the temporal growth rate of ℓ_r as a function of the perturbation wave number k. Here, we have compared, for each configuration, the imposed wavelength against the observed wavelength. When λ_i is comprised between $\lambda_{\max}$ (solid vertical line) and λ_c (dashed vertical line), the observed wavelength matches the imposed one. This cannot be satisfied when $\lambda_i < \lambda_c$ (gray cross), where coarsening occurs and the observed wavelength falls between λ_m and λ_c. Finally, when $\lambda_i > \lambda_{\max}$, rivulet coarsening might also occur [Fig. 10(c)] and the

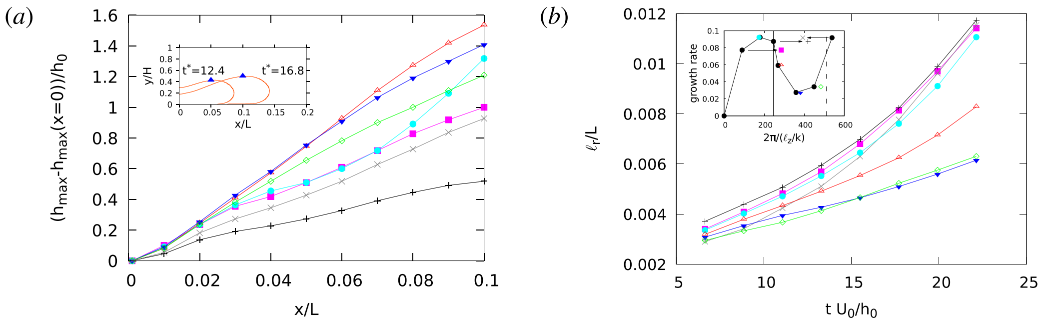

FIG. 11. Growth rate of the perturbation for a vertical film of fluid A with $\mathrm{Re}_l = 7.3$, $\mathrm{Ca} = 0.07$, $\theta_s = 82^\circ$, and $\ell_z/h_0 = 63.6$. (a) Dimensionless maximum film thickness $\max[h(x_0, z_0, t)]$ for different streamwise positions (z_0 always coincides with the initial perturbation tip closer to the domain center) by varying the spanwise wave number: $k = 0$ (plus), $k = 1$ (square), $k = 2$ (circle), $k = 3$ (up-pointing triangle), $k = 4$ (down-pointing triangle), $k = 5$ (empty diamond), $k = 6$ (cross). The inset shows how $h_{\max}$ is computed at two different streamwise positions. (b) Time evolution of the root displacement by varying the initial forcing of the contact line as $\epsilon \cos(2\pi\, k\, z/\ell_z)$. $k = 2$ (circle), $k = 3$ (up-pointing triangle), $k = 4$ (down-pointing triangle), $k = 5$ (empty diamond), $k = 0$ (plus), $k = 1$ (square), $k = 6$ (cross). The inset shows the exponential growth as a function of $2\pi k/\ell_z$. Here, the solid vertical line marks the most unstable wavelength, whereas the dashed line marks the cutoff wavelength.

observed wavelength is closer to the maximum wavelength. We conclude this section by evaluating the effect of an applied phase shift to the initial perturbation of the contact line. For this, we consider the configuration with $k = 4$ [Fig. 10(e)] and apply a perturbation of the form $\epsilon \cos(2\pi\, k\, z/\ell_z + \chi)$, with $\chi = \pi/2$. Figure 12 compares the time evolution of the finger dynamics with and without phase shift. The applied phase shift is characterized by an inflection point at the left and right boundaries of the liquid inlet. Figure 12 shows coarsening in the configuration with phase shift where the perturbed contact line is concave in the vicinity of the inflection point. Here, the liquid structure growing at the boundary merges with the first-forming rivulet, causing the formation of a larger finger which progresses slower than the others (first and second panels from the left). This lateral finger eventually catches the central rivulets (third panel from the left) and then overtakes them to chase its twin (rightmost panel).

C. Influence of contact angle

In this section, we discuss the role of the contact angle on the film stability. For this, we first consider the configuration shown in Figs. 2(i)–2(l), i.e., the case with fluid A, $\mathrm{Re}_l = 2.92$, $\mathrm{Ca} = 0.04$, $\ell_z/h_0 = 121.2$, and $\theta_s = 82.5^\circ$. For this case we have studied three additional contact angles: $\theta_s = (40^\circ, 120^\circ, 160^\circ)$. We have found that the cascade and the number of the observed rivulets is not affected by the contact angle. Indeed, all the new studied cases show six rivulets, which develop from a side-to-center cascade of three couples. This is shown in Fig. 13. However, the contact angle has an effect on the average wavelength λ. Table IV shows that λ decreases with increasing θ_s. This is mainly due to the decrease in film width, which is more pronounced for high values of θ_s (last column of Table IV), finishing by reducing the distance between each couple of rivulets.

D. Summary of wavelength selection

In this section we discuss the wavelength selection results for all the simulated cases with fluid A. By neglecting the decrease in film width, we aim at establishing whether the distance between fingers matches the most unstable wavelength predicted by linear theory, despite the fact that the

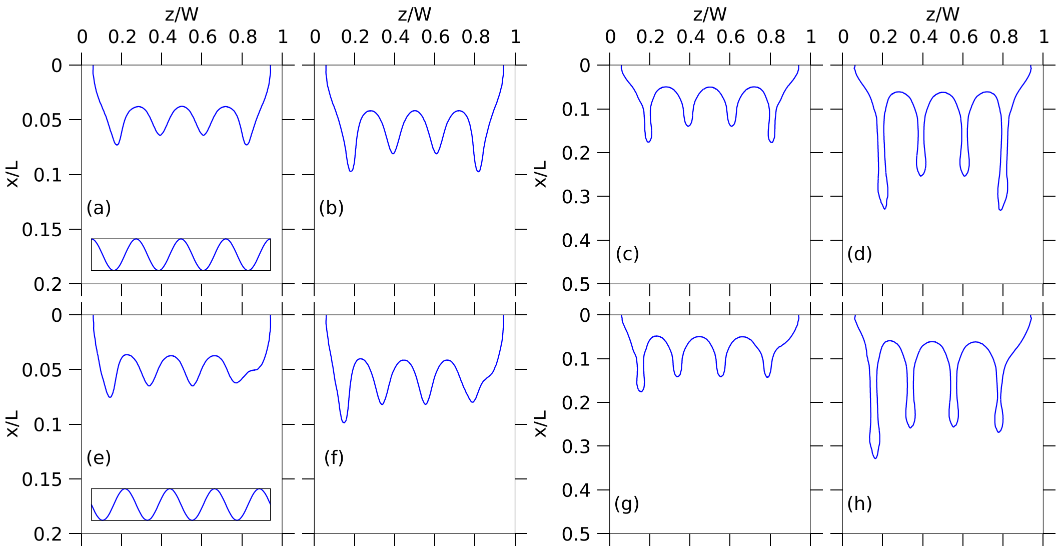

FIG. 12. Snapshots of the contact-line dynamics in a vertical film of fluid A at $\mathrm{Re}_l = 7.3$, $\mathrm{Ca} = 0.07$, $\theta_s = 82^\circ$, and $\ell_z/h_0 = 63.6$. Influence of phase shift in the perturbed initial condition (represented in the inset of the leftmost panels, whose amplitude is intentionally not to scale): $\epsilon\cos(2\pi\, k\, z/\ell_z + \chi)$ with $\chi = 0$ (top) and $\chi = \pi/2$ (bottom). Time evolution of finger dynamics from left to right: $t^\star = 11$; $t^\star = 13.3$; $t^\star = 17.7$; $t^\star = 22$.

instability develops in cascade and that the film is not in contact with sidewalls. This condition can be expressed as

$$n - 1 = \frac{\ell_z}{\lambda_{\max}}, \tag{31}$$

where n is the number of observed rivulets. By replacing $\lambda_{\max}$ with Eq. (29), we can write

$$n = \frac{\ell_z(3\mathrm{Ca})^{1/3}}{h_0}\frac{1}{\kappa} + 1. \tag{32}$$

Figure 14 summarizes the number of observed rivulets for all the considered scenarios. Symbols refer to our DNS results, whereas lines represent the prediction of several models: Johnson *et al.*

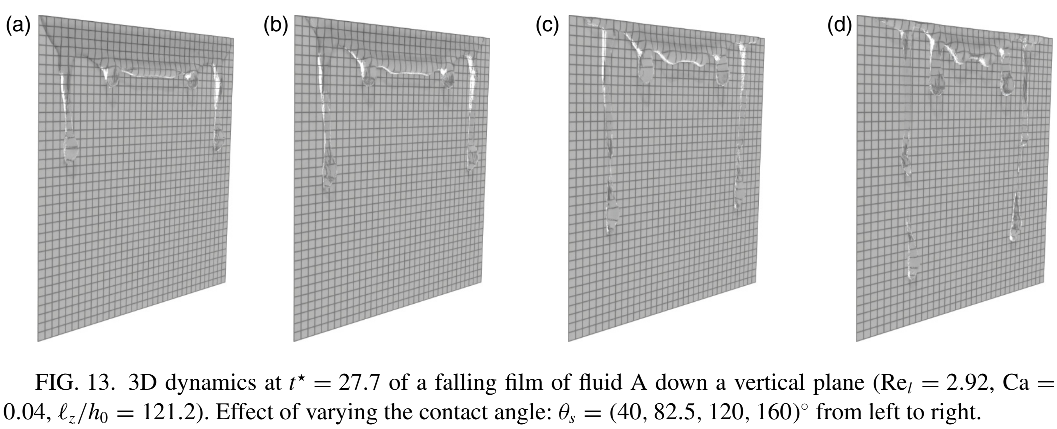

FIG. 13. 3D dynamics at $t^\star = 27.7$ of a falling film of fluid A down a vertical plane ($\mathrm{Re}_l = 2.92$, $\mathrm{Ca} = 0.04$, $\ell_z/h_0 = 121.2$). Effect of varying the contact angle: $\theta_s = (40, 82.5, 120, 160)^\circ$ from left to right.

TABLE IV. Rivulet number n, observed wavelength and width restriction by varying the contact angle. Scenario of Figs. 2(i)–2(l): fluid A, Re = 2.92, Ca = 0.04, $\ell_z/h_0 = 121.2$.

θ_s (deg)	n	λ_I (mm)	λ_{II} (mm)	λ_{III} (mm)	$\lambda/\lambda_{\max}$	Ψ (deg)
40	6	77	42	17	0.7	33
82.5	6	75	41	16	0.65	45
120	6	67	40	15	0.58	52
160	6	62	36	14	0.54	79

[8] (green line), Troian *et al.* [38] (black line), Silvi and Dussan [5] (red line), Huppert [4] (blue line). We have also represented the cutoff wavelength (dashed line) (Kondic and Diez [16]). The simulated cases differ from each other either by varying ℓ_z/h_0 (empty square), or by varying Re_l and Ca (all remaining symbols). It turns out that all simulated cases generate rivulets which separate each other more than the cutoff wavelength and in line with the prediction of linear instability.

V. CONCLUSIONS

By employing 3D direct numerical simulations, we have studied a falling film of partially wetting fluid down a vertical plane in the presence of air. We have focused on conditions where the film is not in contact with sidewalls. In this configuration, two contact lines develop at the sides and the film width decreases due to the effect of surface tension (Lan *et al.* [19], Thoraval *et al.* [20]). We have demonstrated that accounting for inertia in the balance of forces in the normal direction to the contact line is essential to correctly predict the decrease in film width, particularly when Re Bo > 2 [Fig. 6(b)].

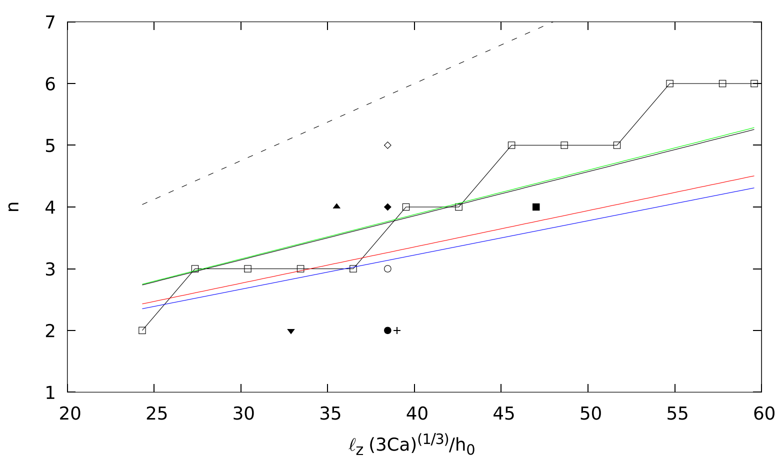

FIG. 14. Number of observed rivulets for all simulated cases with fluid A and comparison with linear stability predictions of several models: Johnson *et al.* [8] (green line), Troian *et al.* [38] (black line), Silvi and Dussan [5] (red line), Huppert [4] (blue line); the dashed line marks the cutoff wavelength (Kondic and Diez [16]); results of simulated cases are represented by symbols: scenarios with inlet width varied (empty square); scenario $\mathrm{Re}_l = 30$ (down-pointing triangle); scenario $\mathrm{Re}_l = 15$ (up-pointing triangle); scenario $\mathrm{Re}_l = 7.3$ ($k = 0, 1, 2$ filled circle; $k = 3$ empty circle; $k = 4, 6$ filled diamond; $k = 5$ empty diamond); scenario $\mathrm{Re}_l = 1.2$ (filled square); scenario $\mathrm{Re}_l = 6.47$ (plus).

The width restriction causes the liquid to accelerate toward the center. As a consequence, two twin rivulets develop at the sides. The liquid is prone to flow within the rivulet and generates a stagnation zone at the front advancing contact line (Fig. 7). This is the beginning of a new contact-line instability which triggers the formation of a new couple of twin fingers (if the distance between the lateral fingers is large enough). This feeds the instability mechanism again and activates the finger cascade (Fig. 2).

By applying an initial sinusoidal shape perturbation of the contact line, the rivulet cascade is suppressed when the wavelength of the imposed perturbation is slightly larger than the cutoff wavelength predicted by linear instability. In this case, all the central rivulets appear at the same time and develop simultaneously by exhibiting the same length [Fig. 10(f)]. Nevertheless, applying an initial perturbation of the contact line fosters the instability growth rate [Fig. 11(a)] and the speed of the rivulet roots [Fig. 11(b)]. We have also identified three regimes: (i) if the perturbation wavelength λ_i lies between λ_c and $\lambda_{\max}$, the number of observed rivulets is consistent with the perturbation [Figs. 10(d)–10(f)]; this is no longer the case when (ii) the perturbation wavelength is shorter than λ_c [Fig. 10(g)] and when (iii) is greater than $\lambda_{\max}$ [Figs. 10(a)–10(c)].

However, even though the fingering instability follows a cascade and the film is not attached to the sidewalls, for all the simulated scenarios, the selected wavelength (average distance between rivulets) is in agreement with the unstable band predicted by linear stability results obtained via the lubrication approximation [16,38]. In particular, the shortest attainable distance between observed rivulet is always larger than the cutoff wavelength (Fig. 14).

Nevertheless, the average wavelength is affected by inertia and by film thickness. Indeed, for large Reynolds number and for large film thicknesses, the decrease in film width is less pronounced and, as a result, the average wavelength between the external rivulets is larger (Fig. 4). The same behavior occurs also at low contact angles (Fig. 13).

ACKNOWLEDGMENTS

This work is funded by the STAE foundation through the reMOVEICE project. G.L. acknowledges A. Pedrono and P. Elyakime for support with the code JADIM, and M. Pigou for support with the generation of 3D figures. The authors also acknowledge L. Bennani and P. Trontin for stimulating discussions. Helpful comments by the two anonymous referees are gratefully acknowledged. This work was granted access to the HPC resources of CALMIP supercomputing center under Allocation No. 2019-P1519, and of CINES under the Allocation 2019-A0062B10356 attributed by GENCI.

APPENDIX: VALIDATION OF JADIM IN THE SPREADING FILM SCENARIO

In order to validate the numerical code JADIM in the spreading film configuration, we start by performing a mesh grid sensitivity analysis. We consider one representative case studied in this work, i.e., the scenario of Figs. 2(i)–2(l). Here, a vertical film of partially wetting fluid (fluid A in Table I) falls on a vertical wall at $\mathrm{Re}_l = 2.92$, $\mathrm{Ca} = 0.04$, $\theta_s = 82.5^\circ$, $\ell_z/h_0 = 121.2$. The computational domain is 0.1 m long (L), 0.006 m high (H), and 0.1 m wide (W).

The chosen reference grid is composed of 3.2×10^6 uniform cells ($200 \times 80 \times 200$ along x, y, z). With reference to Eqs. (10) and (11), the employed grid provides 12 cells within the waveless film thickness. For all studied cases, we always ensure having at least 12 cells within the waveless film, at least 6 cells within the rivulet width, and at least 20 cells within the rivulet thickness. Since the domain height is much smaller than the domain length and width, and given that we employ at least 12 cells in the waveless film, the use of cubic cells would be too challenging for computational resources. We therefore employ elongated cells for which $\Delta_x = \Delta_z > \Delta_y$. For this representative case, we have $\Delta_x = \Delta_z = 6.7\,\Delta_y$. With the mesh grid sensitivity analysis, we have studied also the effect of the cell elongation.

TABLE V. Grids employed for the convergence analysis shown in Fig. 15 and values of the most important parameters ($t^\star = 24.4$): distance between rivulets λ_I and λ_{II}, rim thickness $h_{\rm rim}$, rivulet thickness $h_{\rm tip}$ and length $\ell_{\rm riv}$, root length ℓ_r, width restriction angle Ψ, capillary number of the lateral contact line Ca_{cl}.

Mesh	$10^{-6}N_{\rm cell}$	$\Delta_{x/z}/\Delta_y$	λ_I (mm)	λ_{II} (mm)	$h_{\rm rim}$ (mm)	$h_{\rm tip}$ (mm)	$\ell_{\rm riv}$ (mm)	ℓ_r (mm)	Ψ (deg)	Ca_{cl}
1	1.28	10.6	72	44	1.31	5.27	45.5	7.1	40	−0.027
2	3.2	6.7	75.5	43	1.23	4.83	32.2	7.2	41	−0.023
3	8	4.2	76	43	1.25	4.67	29.1	7.5	42	−0.023
4	20	2.7	76	43	1.21	4.58	26.2	7.6	44	−0.023
5	49.2	1.7	76	43	1.19	4.48	26.0	7.6	45	−0.023
6	40	5.4	76	43	1.21	4.75	26.1	7.4	43	−0.023

All the grids employed in this analysis are listed in Table V. From mesh 1 to mesh 5, we have gradually increased the number of cells by 2.5 times, keeping Δ_y fixed and decreasing Δ_x and Δ_z simultaneously. Thus, from mesh 1 to mesh 5, the elongation of the cells is less pronounced. In addition to these five grids, we have studied one additional grid (mesh number 6 in Table V) by doubling the number of cells in the y direction with respect to the mesh 4. This last mesh allows us to analyze the effect of the cell elongation.

Figure 15(a) shows the top view of the falling film. All grids, except the coarsest mesh (mesh 1), provide a similar pattern, in particular in the region before the front ridge. This is shown in Fig. 15(b), which depicts the front view of the advancing rim [view along the horizontal line in Fig. 15(a)]. However, achieving convergence for the rivulet speed is much harder (the coarser the grid, the quicker the rivulet): a proper convergence is obtained only with 20×10^6 cells (mesh 4). This is shown in Fig. 15(c), which depicts the rivulet along the vertical dashed line in Fig. 15(a). Here, mesh 4 (green line) and mesh 5 (black line) provide full convergence. Nevertheless, we have collapsed, by shifting the time, the rivulets resulting from different grids in Fig. 15(d). This gives the shape of the rivulet when it passes by the same streamwise position: a satisfactory agreement is

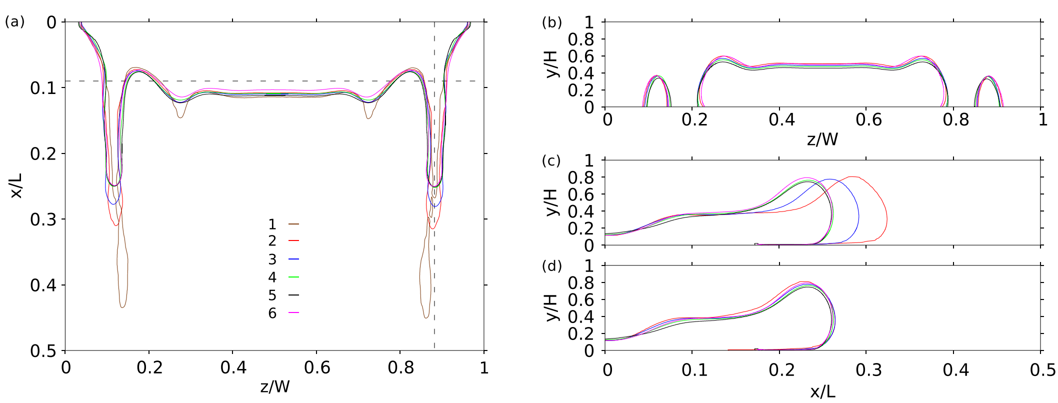

FIG. 15. Grid dependence analysis showing a falling film of fluid A down a vertical wall ($\mathrm{Re}_l = 2.92$, $\mathrm{Ca} = 0.04$, $\theta_s = 82.5^\circ$, $\ell_z/h_0 = 121.2$) at $t^\star = 24.4$. Comparison of six different meshes, whose details are given in Table V. (a) Top view (cut in the plane xz at $y = 0.0005$ m). The dashed lines mark the cuts shown in panels (b) and (c). (b) Front view [cut in the plane yz at $x/L = 0.09$, horizontal line in panel (a)]. (c) Side view of the lateral rivulet [cut in the plane xy at $z/w = 0.88$, vertical line in panel (a)]. (d) Side view of the rivulet shown in panel (c) at the moment where they are at the same position. Mesh 1 gives inconsistent results and therefore is not shown in panels (b), (c), (d).

TABLE VI. Wavelength of the instability as a function of inclination angle β and Reynolds number Re_l, for a film of fluid B as defined in Johnson *et al.* [8] and $\theta_s = 47^\circ$. Comparison between experimental results of Johnson *et al.* [8], defined here as λ_J, and our average wavelength λ from DNS.

β (deg)	Re_l	Ca	λ_J (mm)	λ (mm)
90	0.13	0.020	20 ± 5	16.7
90	0.51	0.049	21 ± 5	18.2

observed for all grids, suggesting that is harder to achieve convergence for the rivulet speed rather than the rivulet shape.

Finally, the analysis of mesh 6 serves to discuss the effect of the cell elongation. We have doubled the number of cells of mesh 4, i.e., the coarser grid providing full convergence, by doubling the number of cell in the y direction only. From the analysis of Figs. 15(a) and 15(c), mesh 6 (purple line) lacks in capturing the correct rivulet width while captures well the rivulet thickness, although it has more cells than mesh 4 in the y direction and the same number of cells along x and z.

Table V lists the most important parameters used in the paper. Meshes 2–6 give similar results in terms of the general flow dynamics, except for the rivulet length, whose convergence is achieved starting from mesh 4. In particular, the reference grid (mesh 2 in Table V and red line in Fig. 15) captures well the distance between rivulets (λ_I and λ_{II}), as well as the width restriction and the movement of the lateral contact line (ψ and Ca_{cl}). Also, since the qualitative behavior of the general dynamics is still well captured, we can conclude that the reference simulation is a good compromise between accuracy of results and computational cost. As a result, all simulated cases throughout the paper are characterized by the same cell size (Δ_x, Δ_y, Δ_z) as the reference grid.

We now move to the validation of the code JADIM by studying the rivulet wavelength, defined as the distance between rivulets. We compare our numerical results with the experimental data by Johnson *et al.* [8], who measured experimentally, among the others, the wavelength of the instability as a function of Re_l and β. The working liquid is the fluid B in Johnson *et al.* [8] (80% water-glycerin mixture). The imposed contact angle is $\theta_s = 47^\circ$. We have focused on two configurations, whose parameters are listed in Table VI. In order to eliminate the effect of the side contact lines, we have performed these two simulations with a larger computational width ($W = 0.2$ m) and by forcing the liquid film to touch the sidewalls. By doing so, $\ell_z = W$. No contact-line perturbation is applied.

The average rivulet distance λ resulting from our DNS data is listed in Table VI, which shows a good agreement with the experimental analysis, Eq. (29). Figure 16 depicts the 3D view of the liquid film for the scenario at $\mathrm{Re}_l = 0.13$ (first line in Table VI). The formed fingers are characterized by nonuniform lengths, as observed also by Johnson *et al.* [8]. The small computational domain, which can accommodate only some wavelengths, certainly plays a role on this.

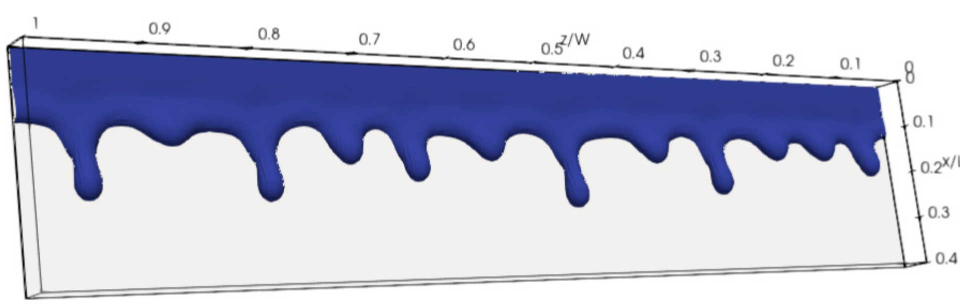

FIG. 16. 3D view of a falling film with sides attached to the lateral walls down a vertical plane (0.1 m long and 0.2 m wide) at $\mathrm{Re}_l = 0.13$.

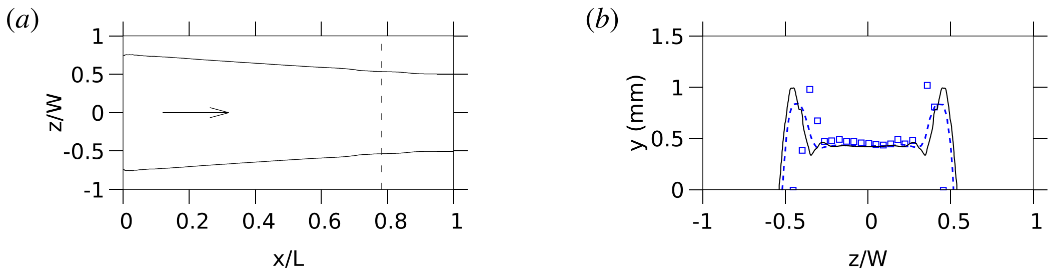

FIG. 17. Falling film spreading on a vertical wall: $\mathrm{Re}_l = 266$, $\mathrm{Ca} = 0.015$, $\theta_s = 30^\circ$, $\ell_z = 7.62$ cm. (a) Width restriction from our DNS. The dashed line marks the plane located at 10 cm from the inlet, where the film thickness profile is computed in (b). The arrow indicates the flow direction. (b) Film thickness profile. Comparison of our DNS (solid line) with Lan *et al.* [19] (dashed line: numerical; square: experimental).

To conclude the validation section, we analyze a situation where the film is not attached to the lateral walls. This is a feature of all the simulated cases throughout the paper. We compare our numerical results of the decrease in film width to the experimental and numerical work of Lan *et al.* [19]. In their Fig. 13, the authors show the measured and simulated film thickness for several different conditions by employing water surfactant as working fluid. We have reproduced the case of their Fig. 13(b) (top): $\beta = 90^\circ$, $\mathrm{Re}_l = 266$, $\mathrm{Ca} = 0.015$, $\theta_s = 30^\circ$. The imposed inlet width is $\ell_z = 7.62$ cm. Figure 17(a) shows the film flow and the width restriction from our simulation. The dashed line, located at 10 cm from the inlet, marks the position where the film thickness profile is computed in Fig. 17(b). Here, we have also represented the experimental (square) and numerical (dashed line) data of Lan *et al.* [19]. The agreement in film width, thickness, and lateral ridge thickness is good. In particular, the lateral ridge thickness from our DNS is closer to the experimental data than the numerical curve of Lan *et al.* [19].

[1] B. E. Thompson and J. Jang, Aerodynamic efficiency of wings in rain, J. Aircraft **33**, 1047 (1996).
[2] M. Spaid and G. Homsy, Stability of Newtonian and viscoelastic dynamic contact lines, Phys. Fluids **8**, 460 (1996).
[3] D. Bonn, J. Eggers, J. Indekeu, J. Meunier, and E. Rolley, Wetting and spreading, Rev. Mod. Phys. **81**, 739 (2009).
[4] H. Huppert, Flow and instability of a viscous current down a slope, Nature (London) **300**, 427 (1982).
[5] N. Silvi and E. Dussan V, The rewetting of an inclined solid surface by a liquid, Phys. Fluids **28**, 5 (1985).
[6] J. M. Jerrett and J. R. de Bruyn, Fingering instability of a gravitationally driven contact line, Phys. Fluids A: Fluid Dyn. **4**, 234 (1992).
[7] J. R. de Bruyn, Growth of fingers at a driven three-phase contact line, Phys. Rev. A **46**, R4500(R) (1992).
[8] M. F. G. Johnson, R. A. Schluter, M. J. Miksis, and S. G. Bankoff, Experimental study of rivulet formation on an inclined plate by fluorescent imaging, J. Fluid Mech. **394**, 339 (1999).
[9] L. Kondic and J. Diez, Pattern formation in the flow of thin films down an incline: Constant flux configuration, Phys. Fluids **13**, 3168 (2001).
[10] R. Ledesma-Aguilar, A. Hernández-Machado, and I. Pagonabarraga, Dynamics of driven three-dimensional thin films: From hydrophilic to superhydrophobic regimes, Phys. Fluids **20**, 072101 (2008).
[11] J. A. Diez and L. Kondic, Contact Line Instabilities of Thin Liquid Films, Phys. Rev. Lett. **86**, 632 (2001).
[12] D. Moyle, M.-S. Chen, and G. Homsy, Nonlinear rivulet dynamics during unstable wetting flows, Int. J. Multiph. Flow **25**, 1243 (1999).
[13] M. H. Eres, L. W. Schwartz, and R. V. Roy, Fingering phenomena for driven coating films, Phys. Fluids **12**, 1278 (2000).

[14] R. Ledesma-Aguilar, R. Nistal, A. Hernández-Machado, and I. Pagonabarraga, Controlled drop emission by wetting properties in driven liquid filaments, Nat. Mater. **10**, 367 (2011).

[15] D. Sebastia-Saez, S. Gu, and M. Ramaioli, Effect of the contact angle on the morphology, residence time distribution and mass transfer into liquid rivulets: A CFD study, Chem. Eng. Sci. **176**, 356 (2018).

[16] L. Kondic and J. Diez, Instabilities in the flow of thin films on heterogeneous surfaces, Phys. Fluids **16**, 3341 (2004).

[17] J. Marshall and S. Wang, Contact-line fingering and rivulet formation in the presence of surface contamination, Comput. Fluids **34**, 664 (2005).

[18] D. Slade, S. Veremieiev, Y. Lee, and P. Gaskell, Gravity-driven thin film flow: The influence of topography and surface tension gradient on rivulet formation, Chem. Eng. Process. **68**, 7 (2013).

[19] H. Lan, J. L. Wegener, B. F. Armaly, and J. A. Drallmeier, Developing laminar gravity-driven thin liquid film flow down an inclined plane, ASME J. Fluids Eng. **132**, 081301 (2010).

[20] B. Thoraval, J. Lallement, P. Berthoumieu, C. Laurent, and P. Gajan, An experimental study on gravity-driven film: Influence of viscosity, wall surface treatment and transitory state, in *10th International Conference on Multiphase Flow (ICMF)*, 2019, Rio de Janeiro, Brazil.

[21] J. Lallement, Modélisation et simulation numérique d'écoulements de films minces avec effet de mouillage partiel, Ph.D. thesis, ISAE, 2019 .

[22] C. Huh and L. E. Scriven, Hydrodynamic model of steady movement of a solid/liquid/fluid contact line, J. Colloid Interf. Sci. **35**, 85 (1971).

[23] O. V. Voinov, Hydrodynamics of wetting, Fluid Dyn. **11**, 714 (1976).

[24] R. G. Cox, The dynamics of the spreading of liquids on a solid surface. Part 1. Viscous flow, J. Fluid Mech. **168**, 169 (1986).

[25] J. Magnaudet, M. Rivero, and J. Fabre, Accelerated flows past a rigid sphere or a spherical bubble. Part 1. Steady straining flow, J. Fluid Mech. **284**, 97 (1995).

[26] D. Legendre and J. Magnaudet, The lift force on a spherical bubble in a viscous linear shear flow, J. Fluid Mech. **368**, 81 (1998).

[27] T. Bonometti and J. Magnaudet, An interface-capturing method for incompressible two-phase flows: Validation and application to bubble dynamics, Int. J. Multiph. Flow **33**, 109 (2007).

[28] J.-B. Dupont and D. Legendre, Numerical simulation of static and sliding drop with contact angle hysteresis, J. Comput. Phys. **229**, 2453 (2010).

[29] C. Hirt and B. Nichols, Volume of fluid (VOF) method for the dynamics of free boundaries, J. Comput. Phys. **39**, 201 (1981).

[30] J. Brackbill, D. Kothe, and C. Zemach, A continuum method for modeling surface tension, J. Comput. Phys. **100**, 335 (1992).

[31] S. T. Zalesak, Fully multidimensional flux-corrected transport algorithms for fluids, J. Comput. Phys. **31**, 335 (1979).

[32] H. S. H. Mohand, H. Hoang, G. Galliero, and D. Legendre, On the use of a friction model in a volume of fluid solver for the simulation of dynamic contact lines, J. Comput. Phys. **393**, 29 (2019).

[33] D. Legendre and M. Maglio, Comparison between numerical models for the simulation of moving contact lines, Comput. Fluids **113**, 2 (2015).

[34] W. Nusselt, Der wärmeaustausch am berieselungskühler, VDI-Zeitschrift **67**, 206 (1923).

[35] G. Lavalle, J. P. Vila, G. Blanchard, C. Laurent, and F. Charru, A numerical reduced model for thin liquid films sheared by a gas flow, J. Comput. Phys. **301**, 119 (2015).

[36] J. Sebilleau, L. Lebon, and L. Limat, Dry patches in a flowing film: Predicting rewetting and the effects of inertia, Phys. Fluids **27**, 102106 (2015).

[37] T. Podgorski, J.-M. Flesselles, and L. Limat, Dry arches within flowing films, Phys. Fluids **11**, 845 (1999).

[38] S. Troian, E. Herbolzheimer, S. Safran, and J. Joanny, Fingering instabilities of driven spreading films, Europhys. Lett. **10**, 25 (1989).

[39] G. Lerisson, P. G. Ledda, G. Balestra, and F. Gallaire, Dripping down the rivulet, Phys. Rev. Fluids **4**, 100504 (2019).